



Enhanced shear strength of Cu–Sn intermetallic interconnects with interlocking dendrites under fluxless electric current-assisted bonding process

Baolei Liu¹, Yanhong Tian^{1,*} , Jiayun Feng¹, and Chenxi Wang¹

¹ State Key Laboratory of Advanced Welding and Joining, Harbin Institute of Technology, Harbin 150001, China

Received: 12 August 2016

Accepted: 4 October 2016

Published online:
13 October 2016

© Springer Science+Business
Media New York 2016

ABSTRACT

In this paper, the electric current density of $1.44 \times 10^4 \text{ A cm}^{-2}$ was imposed to assemble Cu/(30 μm) Sn/Cu interconnection systems without flux at ambient temperature to fabricate Cu–Sn interconnects within 180 ms. From the three-dimensional microstructural observation of interfacial intermetallic compounds (IMCs) at different bonding times, the rod-like Cu_6Sn_5 formed at the initial stage was changed into dendritic Cu_6Sn_5 due to constitutional supercooling. When the joule heat-induced temperature was increased above the melting point of Cu_6Sn_5 , the dendritic Cu_6Sn_5 were melted and then totally converted into Cu_3Sn , resulting in the formation of homogeneous Cu_3Sn intermetallic joints. The ultrarapid microstructure evolution of the interfacial IMCs was caused by enhanced solid–liquid interdiffusion kinetics, which can be attributed to the joule heating effect as well as the solid–liquid electromigration of Cu in molten Sn with the passage of electric current. In addition, the mechanical analysis shows that the microstructure changes of interfacial IMCs can strongly influence the shear strength as well as the fracture mechanism of the resulted joints. The dendritic network of Cu–Sn IMCs enhanced the shear strength of resulted joints due to the interlocking effect, meanwhile, the homogeneous Cu_3Sn joint exhibited the highest shear strength of 67.3 MPa.

Introduction

During the soldering process in electronic packaging technology, the formation of interfacial intermetallic compounds (IMCs) between solder and under bump metallization (UBM) is crucial to provide thermal and

electrical conduction, as well as mechanical strength for electronic components [1–3]. Concurrently, with the increasingly shifting from two-dimensional to three-dimensional (3D) integrated circuits in electronic products, the diameter of solder bumps on 3D stacking chips is reducing from present 100 μm to

Address correspondence to E-mail: tianyh@hit.edu.cn

anticipated 1 μm in future. However, the thickness of the UBM remains almost the same as that in flip-chip solder joints [4–6]. As a result, the volume proportion of IMCs to the whole solder bumps is significantly increased, and the solder would be even transformed completely into intermetallic phases after multiple stacking processes [7, 8]. Therefore, the reliability and mechanical property of the miniaturized interconnections are becoming more sensitive to the type, morphology, and volume proportion of interfacial IMCs [9–12].

The binary Cu–Sn system is one of the most commonly used metallurgical options for conventional soldering processes of the interconnection in electronic packaging technology, because of its easy formation of Cu–Sn IMCs such as Cu_6Sn_5 and Cu_3Sn [13–15]. Recent studies for fabricating high-temperature stable Cu–Sn intermetallic interconnects have indicated that Cu_3Sn joint is a more promising candidate used in stacking chips and high-power electronics, because of its higher melting point, lower electrical resistivity, and better mechanical property compared to those of Sn-based solder joints [4, 8, 16–18]. However, the formation of the thermodynamically stable Cu_3Sn joint through conventional solid–liquid interdiffusion (SLID) bonding or transient liquid phase (TLP) soldering process is highly time-consuming [19–21]. The annealing time for completely consuming the residual Cu_6Sn_5 phases and Sn solder are required even up to multiple hours, which will seriously affect the reliability of the packaging systems.

Many commercially reasonable efforts have been made to shorten the bonding time for fabricating the high-melting-point intermetallic interconnects by means of increase in the bonding temperature [20], or ultrasonic-assisted bonding process [16, 17, 22]. Under the elevated temperature or the sonochemical effects of acoustic cavitation, the solid–liquid interdiffusion can be effectively promoted, resulting in the rapid formation of IMCs. Recently, numerous electric current stressing studies of Cu/molten Sn solder/Cu interconnection system have been performed to understand the diffusion behaviors of Cu in molten Sn or Sn-based solder can be significantly enhanced by the electron wind force-induced solid–liquid electromigration (EM), implying a potential way to fabricate full intermetallic joints rapidly. After the electric effect-correlated metallurgy reaction, the interfacial

IMCs with various morphologies and compositions were probably obtained, which is crucial to the mechanical properties of resulted solder joints.

This study focused on the correlation between microstructure and shear property of Cu–Sn interconnects, which were prepared by soldering Cu/Sn/Cu sandwich structures with the assistance of electric current at ambient temperature within several hundred milliseconds (ms). The thermoelectric coupling effect on the interfacial reaction of solid Cu/molten Sn was investigated to understand the ultrafast formation mechanism of interfacial IMCs.

Materials and methods

Sample preparation

Figure 1 shows the experimental setup of electric current-assisted bonding process and the schematic illustration of sandwiched Cu/Sn foil/Cu interconnection system. Three pieces of 99.99 % pure Cu plates with the thickness of 0.5 mm were utilized as base metal substrates. The solder interlayers were two pieces of 99.9 % pure Sn foils with the thickness of 30 μm . The Sn foils and the two upper Cu substrates were cut into $2.5 \times 2.5 \text{ mm}^2$ pieces, while the other piece of Cu substrate was cut into a $10.0 \times 2.5 \text{ mm}^2$ long strip as the lower substrate. The Cu plates and Sn foils were cleaned with a similar procedure in Ref. [19] prior to the bonding process. After cleaning, the two pieces of Sn foils were symmetrically sandwiched between the Cu substrates and placed on a flat SiO_2 substrate as shown in Fig. 1b.

Electric current-assisted bonding process

As shown in Fig. 1a, the bonding process was performed with the Unitek model HF25 inverter-type DC power supply and two specially designed Cu–Cr electrodes with the cross-sectional area of $2.0 \times 2.0 \text{ mm}^2$. The schematic illustration of bonding current waveform is shown in Fig. 1b. The sandwiched interconnection systems were bonded at the peak bonding current of 900 A for different times (40–180 ms). The electron flow (labeled by “ e^- ”) entered the solder joint “A” from the cathode electrode, passed through the lower Cu substrate and solder joint “B,” and exited through the anode

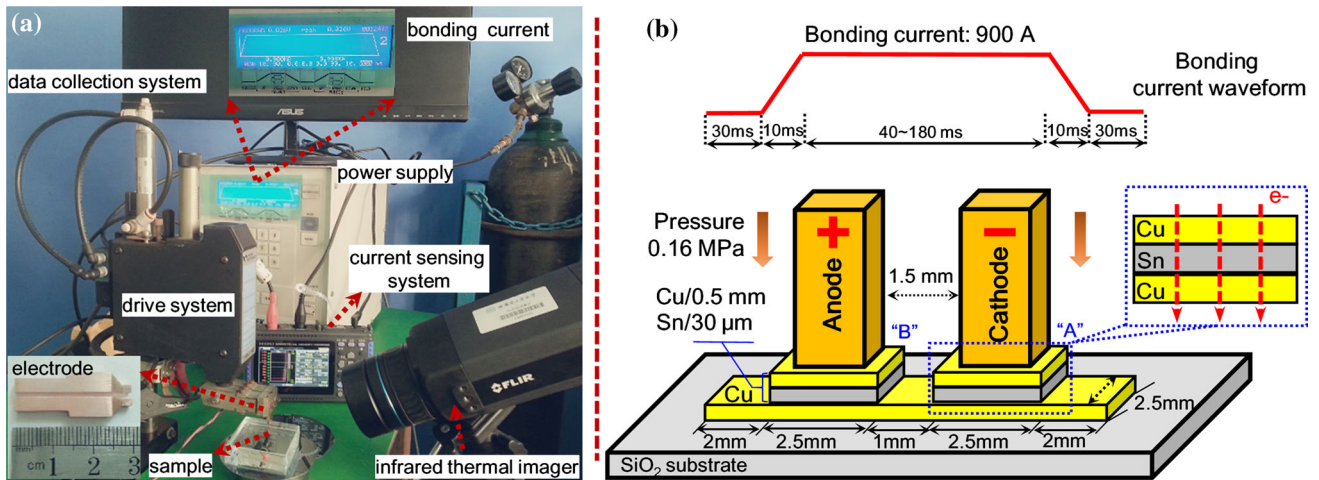


Figure 1 a Experimental setup of electric current-assisted bonding process; b schematic illustration of the Cu/Sn foil/Cu interconnection system.

electrode. Thus, the current density flowing across the $2.5 \times 2.5 \text{ mm}^2$ Sn interlayer was calculated as $1.44 \times 10^4 \text{ A cm}^{-2}$. The pressure supplied by the pneumatically actuated electrodes was 0.16 MPa. Additionally, the real-time temperature of the interconnection system was monitored by an FLIR A615 infrared thermal imaging camera with the emissivity of 0.65. The temperature data were acquired at a rate of 200 frames/s. After the bonding process, two symmetrical solder joints (“A” and “B”) were obtained.

Characterization and shear test

After bonding for different times, one group of samples were carefully ground and polished to the cross-sectional direction. The microstructural evolution was examined by scanning electron microscopy

(SEM). The composition of the Cu–Sn intermetallic phases was identified by energy dispersive X-ray spectroscopy (EDXS), X-ray diffraction (XRD), and transmission electron microscopy (TEM). A dual beam focused ion beam (FIB, FEI Helios Nanolab 600i) was utilized to prepare the TEM specimens. The other group of samples with the same bonding time was prepared for shear tests. As shown in Fig. 2a, b, the shear tests were implemented at room temperature with the shear speed of $200 \mu\text{m/s}$ using a bonding tester (Condor Sigma Lite, XYZTEC). The fracture morphologies were characterized by SEM and EDXS (Fig. 2c). Then, the polished and fractured samples were immersed into a selective etching solution (15 mL vol% HCl + 85 mL deionized water + 5 g FeCl_3) for a certain period of time (3–12 s) to remove the unreacted Sn solder. After the deep-etching procedures, the 3D morphologies of

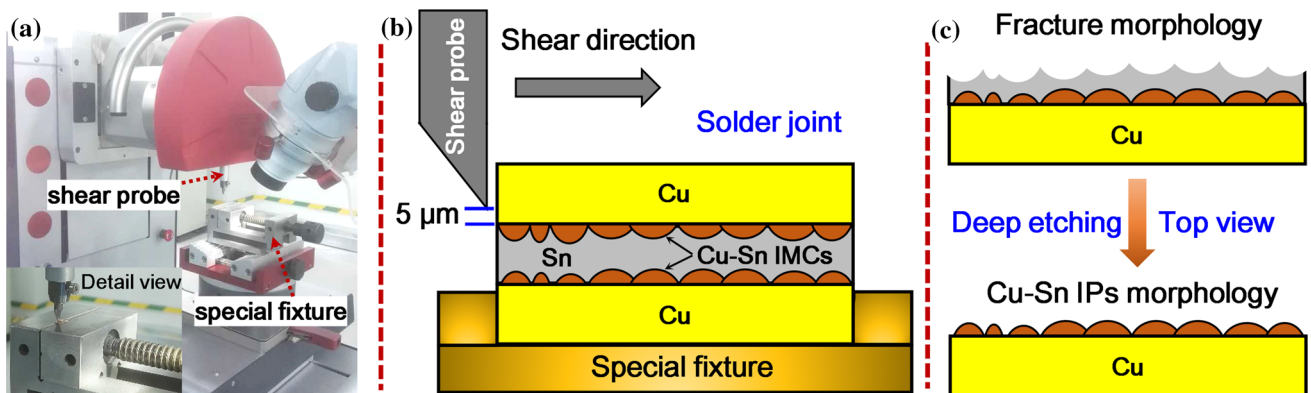


Figure 2 a and b are the experimental setup and schematic illustration of the shear test, respectively; c is the following characterization procedure.

Cu–Sn IMCs can be observed in different directions (longitudinal, transverse, and vertical directions) by using SEM. As shown in Fig. 2c, the top-view can be observed from the longitudinal direction after deep etching the fractured samples. Moreover, the side-view morphologies of unbroken Cu_6Sn_5 grains were observed from the transverse and vertical directions for the deep-etched samples.

Results

Sharply increased bonding temperature

Figure 3 shows the overall temperature profiles of the solder joint “A” and “B” during the electric current-assisted bonding process for 180 ms and the subsequent air cooling procedure. Due to the symmetrical configurations of the interconnection system, the two solder joints had similar temperature profiles. With the onset of the electric current-assisted bonding procedure, the joule heat-induced temperature increased sharply to 232 °C (the Sn melting point) within 40 ms, and then reached the peak temperature of 454 °C (above the melting point of Cu_6Sn_5 , 415 °C) at 150 ms. Thus, the Sn interlayers were certainly melted during the bonding process. After different durations of metallurgical reaction between solid Cu and liquid Sn solder, the as-fabricated solder joints with different microstructures were anticipated.

The initial sharp increase in temperature was attributed to the joule heat generation with the passage of electric current. The heat generation (Q) can be mathematically described as [28]

$$Q = I^2(R_{\text{Contact}} + R_{\text{Cu}} + R_{\text{Sn}} + R_{\text{Electrode}})t, \quad (1)$$

where I is the bonding current and t is the duration of the current application. The resistances include the contact resistance (R_{Contact}) at the faying interfaces of electrode/Cu and Cu/Sn; and the bulk resistances of the Cu plates (R_{Cu}), the Sn foils (R_{Sn}), and the electrodes ($R_{\text{Electrode}}$). The initial static resistance was measured using a digital micro-ohmmeter (ZY9987, Shanghai Zhengyang Instrument) before the bonding current was initiated but after the bonding pressure was applied. The average value of initial static resistances was measured as 11.67 m Ω . Meanwhile, the electrical resistivities of Cu, Sn, and electrode material (Cu–Cr alloy) were 1.7, 11.5, and 2.16 $\mu\Omega$ cm, respectively. The bulk resistance of R_{Cu} , R_{Sn} , and

$R_{\text{Electrode}}$ can be theoretically calculated as 0.126, 0.008, and 0.001 m Ω , respectively. Thus, the majority of the initial static resistance was the contact resistance.

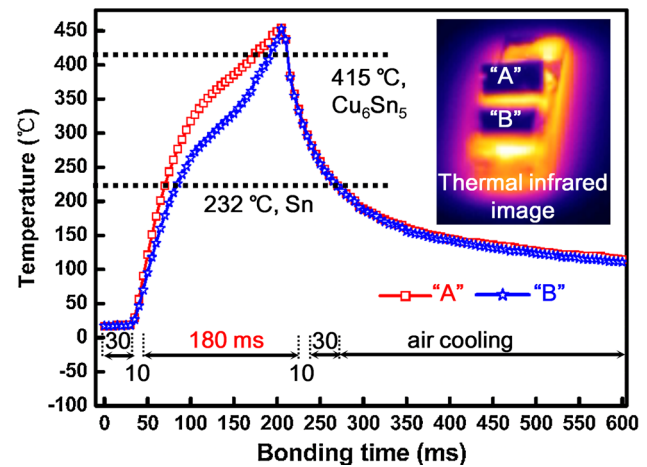


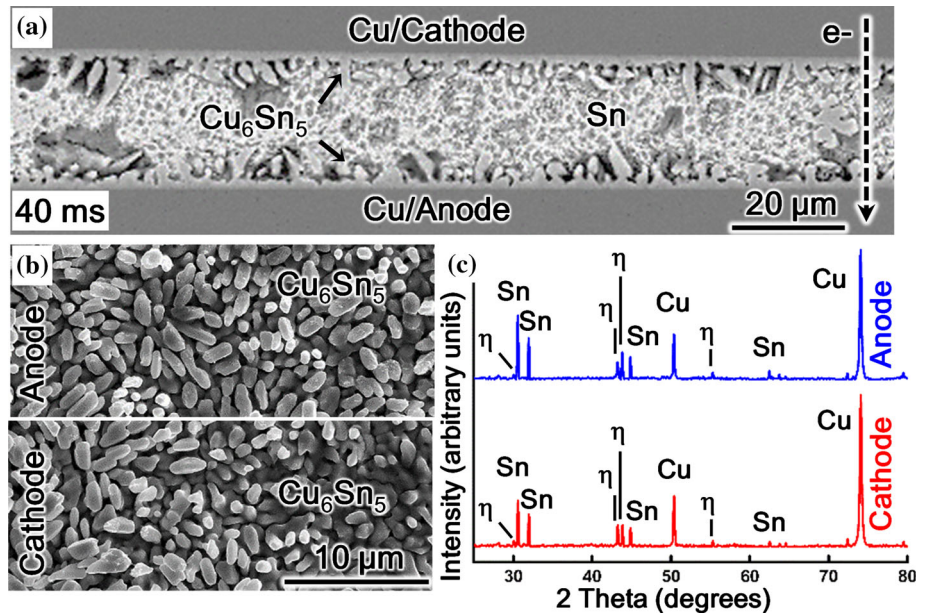
Figure 3 Overall temperature profiles of solder joint A and B during the electric current-assisted bonding process and subsequent air cooling.

tance (R_{Contact}), which was consistent with the measurement in small-scale resistance spot welding of thin Ni sheets [29]. Based on Eq. (1), it is reasonable to consider that the joule heat generation was mainly caused by the larger contact resistances (R_{Contact}) at the initial stage of electric current-assisted bonding process. Besides, no flux was utilized during the bonding process. With the passage of strong electric current, spark plasma was probably generated at the faying Cu/Sn interfaces to remove the surface oxide layer [30, 31]. Meanwhile, as pointed out by Gu et al. [24], the applied electric current can enhance the wetting behavior of molten Sn on Cu substrates.

Microstructure evolution

For conveniently describing the current polarity, only solder joint “A” was analyzed since the structures of solder joint “A” and “B” were symmetric in the assemble interconnection system. Figure 4 shows the SEM images and XRD analyses of the sample after bonding for 40 ms. XRD results, as shown in Fig. 4c, indicated that η - Cu_6Sn_5 phases were formed both at the cathode and anode Cu interfaces. As shown in Fig. 4a, two thin layers of Cu_6Sn_5 compounds formed and adhered well on the Cu substrates. The top-view SEM images in Fig. 4b further show that the 3D morphologies of Cu_6Sn_5 grains at anode and cathode

Figure 4 **a** Cross-sectional SEM image of the solder joint after bonding for 40 ms; **b** top-view SEM images of Cu_6Sn_5 grains on the anode and cathode Cu substrates; **c** XRD analysis of the consisting phases in the solder joint.



Cu substrates are both in short rod-like shape. Moreover, the average grain size of Cu_6Sn_5 at cathode substrate is slightly larger compared to that at anode Cu substrate.

Figure 5 shows the cross-sectional SEM images and the corresponding element distribution maps of the

samples bonded for 60–120 ms. After 60 ms, the joule heat-induced temperature reached 317 °C, resulting in severer interfacial reactions between solid Cu and molten Sn. The cross-sectional SEM images in Fig. 5a show that the morphology of Cu_6Sn_5 seems to be changed into “long rod-like” shape, and randomly

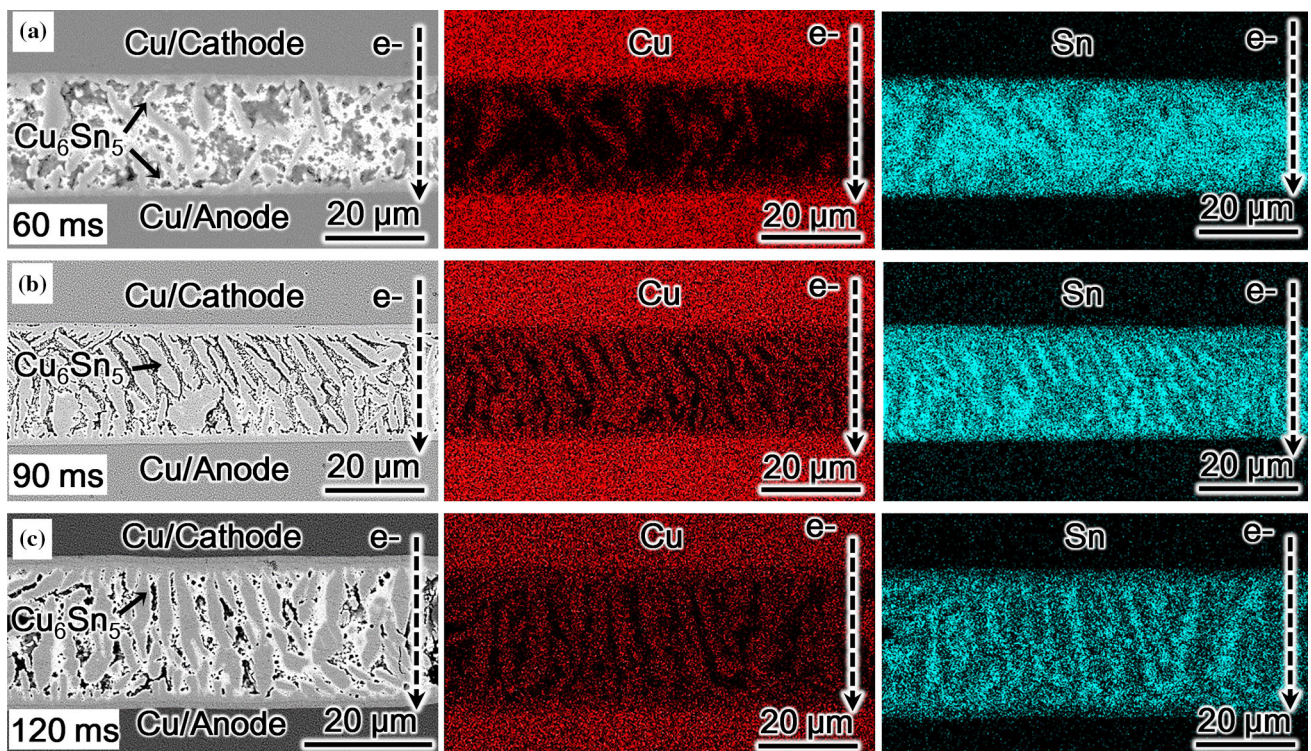


Figure 5 Cross-sectional SEM images and corresponding element distribution maps of the solder joint after bonding for **a** 60 ms, **b** 90 ms, and **c** 120 ms.

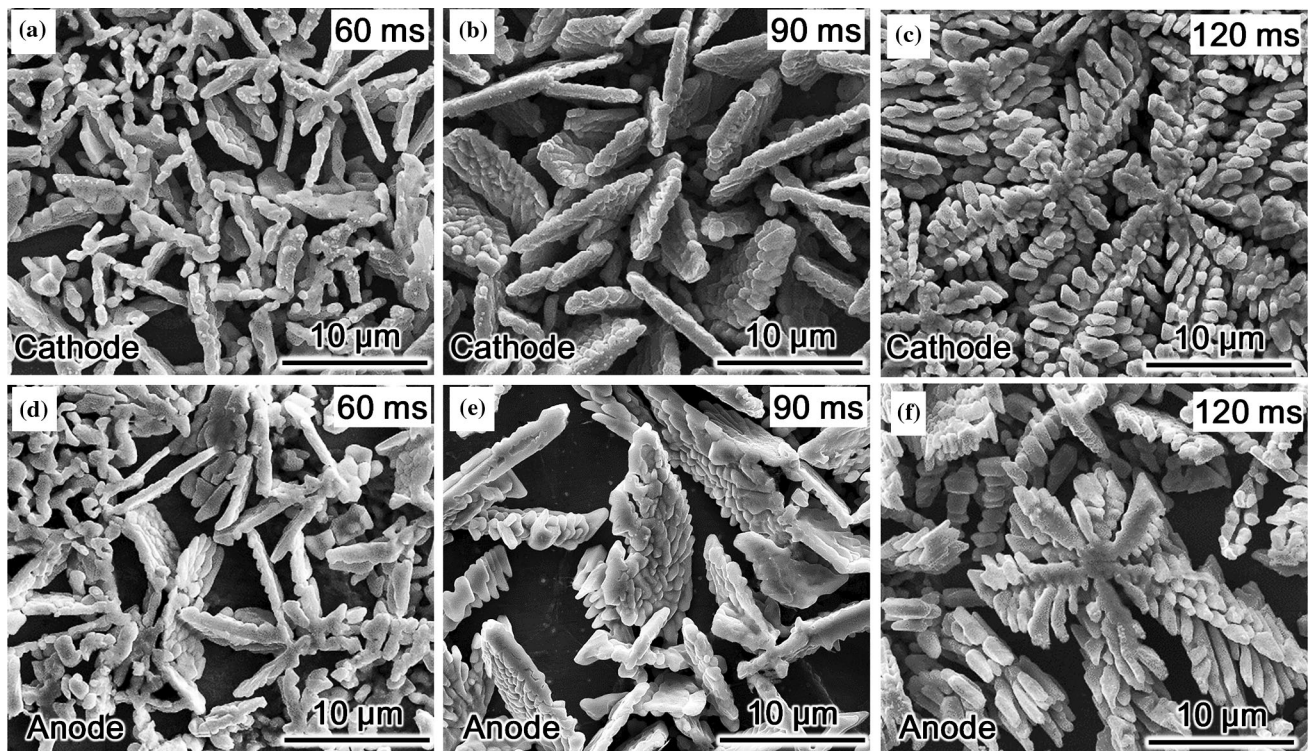


Figure 6 Top-view morphologies of Cu_6Sn_5 grains for different bonding times: **a** cathode, 60 ms; **b** cathode, 90 ms; **c** cathode, 120 ms; **d** anode, 60 ms; **e** anode, 90 ms; **f** anode, 120 ms.

elongated to the Sn solder matrix. After 90 ms, the size as well as the amount of Cu_6Sn_5 grains were both increased (Fig. 5b). The arrangement of these elongated Cu_6Sn_5 grains became more regular, and were almost paralleled with the direction of the downward electron flow. With the bonding time increasing to 120 ms, the Cu_6Sn_5 compounds grew into dendritic shape, and even elongated across the Sn solder interlayer (Fig. 5c).

Figure 6 presents the top-view morphologies of Cu_6Sn_5 grains on cathode and anode Cu substrates after 60–120 ms. At the same bonding times, the Cu_6Sn_5 morphologies at the cathode and anode sides were similar with each other; however, the number of Cu_6Sn_5 grains shows a noticeable difference. The amount of Cu_6Sn_5 grains at cathode was larger compared to that at anode, indicating that the solid-liquid EM of Cu played a significant role in the growth of Cu_6Sn_5 at cathode side. Moreover, the Cu_6Sn_5 morphologies were quite different with the bonding times. As shown in Fig. 6a, d, the actual morphology of Cu_6Sn_5 grains after 60 ms was in platy shape instead of “long rod-like” type. The dimension of the platy Cu_6Sn_5 increased with the bonding time. After 90 ms, small and dense

protuberances were observed on the surface of platy Cu_6Sn_5 grains (Fig. 6b, e). As the bonding time increased to 120 ms, the dendritic Cu_6Sn_5 grains with hierarchical structure of primary- and secondary-branches were formed (Fig. 6c, f).

With the electric current-assisted bonding time further increasing to 150 ms, the bonding temperature induced by joule heat was increased to 454 °C, meaning that the dendritic Cu_6Sn_5 initially formed at the heating up stage (~120 ms) would be melted. Meanwhile, under current stressing, the dissolution of Cu substrates was further enhanced at higher temperature. As a result, the phase composition as well as the morphology of Cu–Sn IMCs would be changed dynamically. As shown in Fig. 7a, after 150 ms, the Sn solder was completely consumed, and the $\text{Cu}_3\text{Sn} + \text{Cu}_6\text{Sn}_5$ intermetallic joint was formed. Based on the EDXS results, the IMCs interlayer was mainly composed of Cu_3Sn dendrites (gray region) interspersed with small-grained Cu_6Sn_5 particles (brighter region). Additionally, a few voids were formed at the Cu/ Cu_3Sn interfaces, which was attributed to the unbalanced diffusion flux of Sn and Cu across Cu_3Sn layer [32–34].

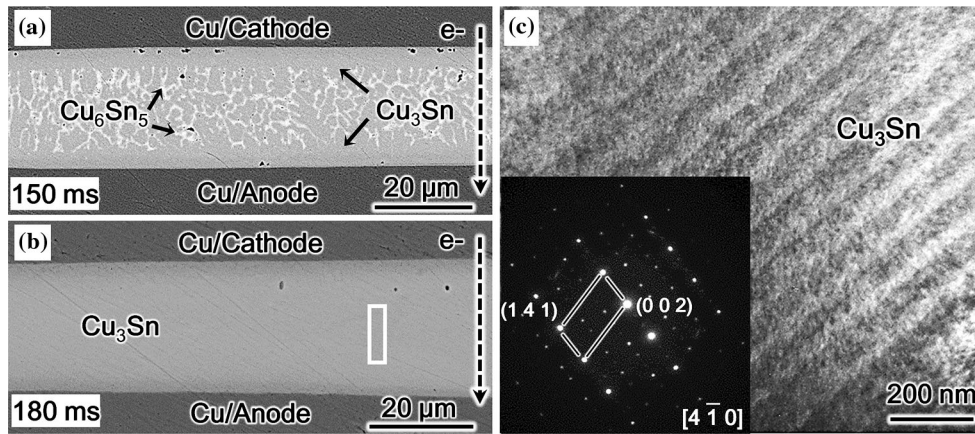


Figure 7 **a** $\text{Cu}_3\text{Sn} + \text{Cu}_6\text{Sn}_5$ intermetallic joint obtained after 150 ms; **b** Cu_3Sn joint obtained after 180 ms; **c** TEM image at the rectangular region in **(b)**, and the typical diffraction pattern of Cu_3Sn .

When the bonding time extended to 180 ms, the small-grained Cu_6Sn_5 particles were totally converted into Cu_3Sn , and then the homogeneous Cu_3Sn joint was obtained, as shown in Fig. 7b. Figure 7c shows the TEM image and the selected area electron diffraction pattern of Cu_3Sn , which was verified by the basic orthorhombic lattice with the dimension of $a = 0.4772 \text{ nm}$, $b = 0.5514 \text{ nm}$, and $c = 0.4335 \text{ nm}$ [35]. Under the electric current-assisted bonding process, the time for forming the homogeneous Cu_3Sn joint was approximately 20 times shorter compared to that under ultrasonic bonding process [16, 17], and was about 5 orders of magnitude faster compared to that under conventional TLP bonding process in previous studies [4, 19, 21]. This ultrafast formation of Cu_3Sn joint was mainly caused by enhanced solid–liquid interdiffusion kinetics, which can be attributed to the joule heating effect as well as the solid–liquid EM of Cu in molten Sn with the passage of electric current.

Shear property

Within 60 ms, the solder joints were mainly composed of residual Sn solder, which were termed as Sn-based solder joints. In the time range of 90–120 ms, the as-fabricated solder joints were composed primarily of dendritic Cu_6Sn_5 , named as Cu_6Sn_5 -based solder joints. After 150 ms, the solder joints were completely transformed into Cu_3Sn -based intermetallic joints. The shear tests were conducted for the samples bonded for 40, 60, 90, 120, 150, and 180 ms.

In general, the shear strengths were increased with the bonding times, as shown in Fig. 8. After 120 ms, the Cu_6Sn_5 -based solder joint with dendritic Cu_6Sn_5 exhibited a robust mechanical property of 52.9 MPa. Meanwhile, the shear strength of the homogeneous Cu_3Sn joint obtained after 180 ms reached the maximum value of 67.3 MPa, which was approximately 200 % higher compared to that of Sn-based solder joint obtained after 40 ms. Therefore, it can be reasonably concluded that the morphology, composition, and proportion of the Cu–Sn IMCs can significantly affect the shear performances of the solder joints. The shear strengths were substantially increased with the volume fraction of Cu–Sn IMCs in the resulted solder joints. This similar conclusion has

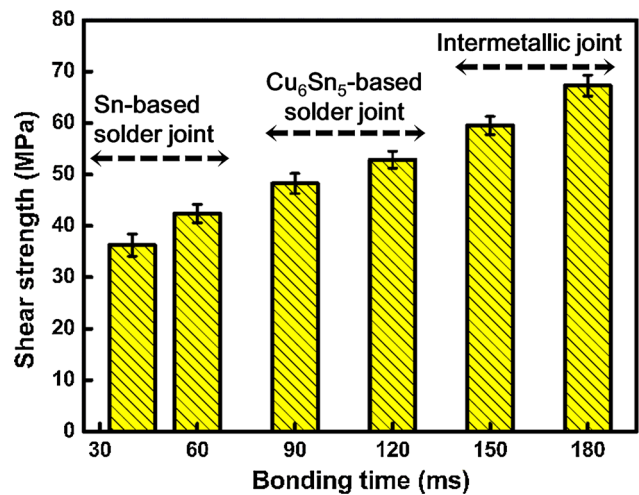


Figure 8 The shear strengths of the as-fabricated joints after different bonding times.

also been systematically reported by Choudhury et al. in Sn-based solder bumps by the means of numerical simulation and experimental analysis [9, 11].

Discussion

Dendritic Cu–Sn IMCs formation under constitutional supercooling

Under the conventional soldering process, the morphology of interfacial Cu_6Sn_5 was usually in scallop-type, which can be explained by the ripening reaction [36]. Meanwhile, the columnar Cu_3Sn grains with layer type were formed by consuming Cu_6Sn_5 phase [19, 21, 37, 38]. However, the formation of dendritic Cu_6Sn_5 and Cu_3Sn grains during the electric current-assisted bonding process indicated that the nucleation and growth behaviors of Cu–Sn IMCs were significantly different from the cases of wetting on the Cu surface under the conventional soldering process. Numerous experimental and theoretical studies of crystal growth from alloy melt have indicated that the redistribution of solute atoms during solidification can cause constitutional supercooling of the melt ahead of an advancing solidification front [39, 40]. The constitutional supercooling would result in a morphological instability of the solid–liquid interface and therefore leads to the formation of dendritic microstructures [41]. The requirement for forming dendrites under constitutional supercooling can be expressed as [42, 43]

$$\frac{G}{R} < mC_0(1 - k_0)/Dk_0, \quad (2)$$

where R is the rate of solidification, G is the temperature gradient, k_0 is the solute distribution coefficient, D is the diffusion coefficient, m is the slope of the liquids, and C_0 is the overall solute concentration. Based on Eq. 2, the increase in solute concentration (C_0) or cooling rate (R) can both increase the degree of constitutional supercooling. Recently, Xian et al. reported formation of dendritic Cu_6Sn_5 in Sn-4 wt% Cu alloy melt under the cooling rate of 1.7 °C/s, which resulted from the high degree of constitutional supercooling in the liquid ahead of solid Cu_6Sn_5 fronts [44].

In this work, the passage of electric current significantly accelerated the dissolution of Cu substrate under the driving force of solid–liquid EM, leading to

the increase of the Cu solute concentration in molten Sn solder. As approximately 14.3- μm thick Cu_6Sn_5 layer was formed after 120 ms, the Cu mass percent in the solder interlayer can be estimated as 17.5 wt%. It was noted that the Cu solute concentration was consistently increased with the bonding times until the solder interlayer was totally transformed into Cu_3Sn . On the other hand, the cooling rate of the bonding system was very high (approximately 880 °C/s) because of the good thermal conductivities of Cu, Sn, and electrode material. Since the Cu solute concentration as well as the cooling rate in the molten Sn solder alloy were larger compared to those in Xian's work, the higher degree of constitutional supercooling generated the liquid ahead of solid Cu–Sn IMCs front. This was the reason for the formation of dendritic Cu–Sn IMCs during the electric current-assisted bonding process.

Enhanced shear strength due to interlocking intermetallic dendrites

In an attempt to explain the enhanced shear strength with bonding times, the typically fractographic morphologies at cathode sides of the Sn-based solder joint (60 ms), Cu_6Sn_5 -based solder joint (120 ms), and Cu_3Sn joint (180 ms) were observed as shown in Fig. 9a–c, respectively. For the Sn-based solder joint, the fractures mainly occurred at the rode-like $\text{Cu}_6\text{Sn}_5/\text{Sn}$ interfaces, which can be both observed at the cathode and anode sides. Figure 9a shows the fractographic morphology of the Sn-based solder joint was in the dimple-like type, which was a mixture fracture mode of brittleness and ductility [45]. It can be seen that the bottom dimple consisted of broken protruding Cu_6Sn_5 tips, and its sides were surrounded by Sn solder. The dimple-like fracture mechanism at $\text{Cu}_6\text{Sn}_5/\text{solder}$ interfaces has been reported by Pang et al. [46], which was attributed to the phase transformation-induced stress and high concentrated stress in the Cu_6Sn_5 layer.

As shown in Fig. 9b, the fracture mode for the Cu_6Sn_5 -based solder joint was still in mixture type. The dendritic Cu_6Sn_5 grains obtained by the electric current-assisted bonding process was usually with a hierarchical structure of primary- and secondary-branches, as clearly shown in Fig. 10. The side-view morphologies of Cu_6Sn_5 , as shown in Fig. 10a, b, were obtained from the polished and fractured samples after deep-etching procedure, respectively.

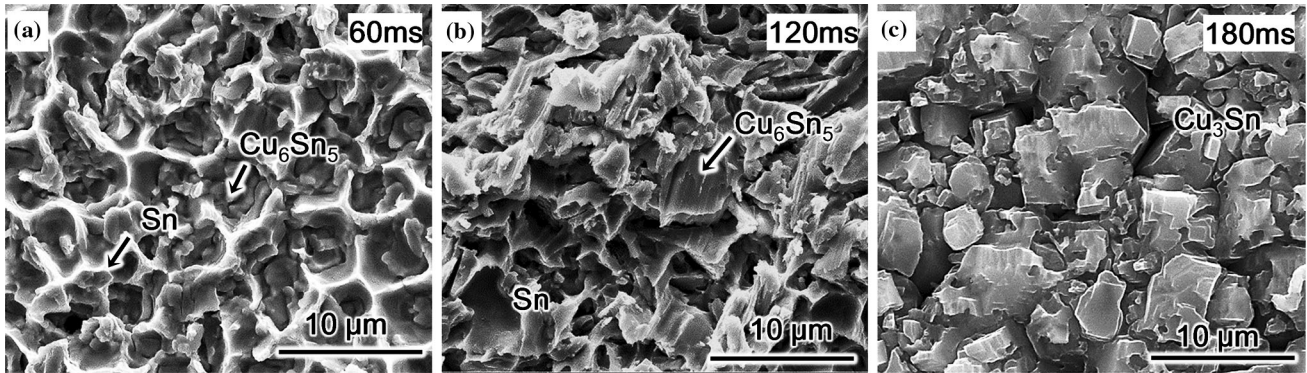
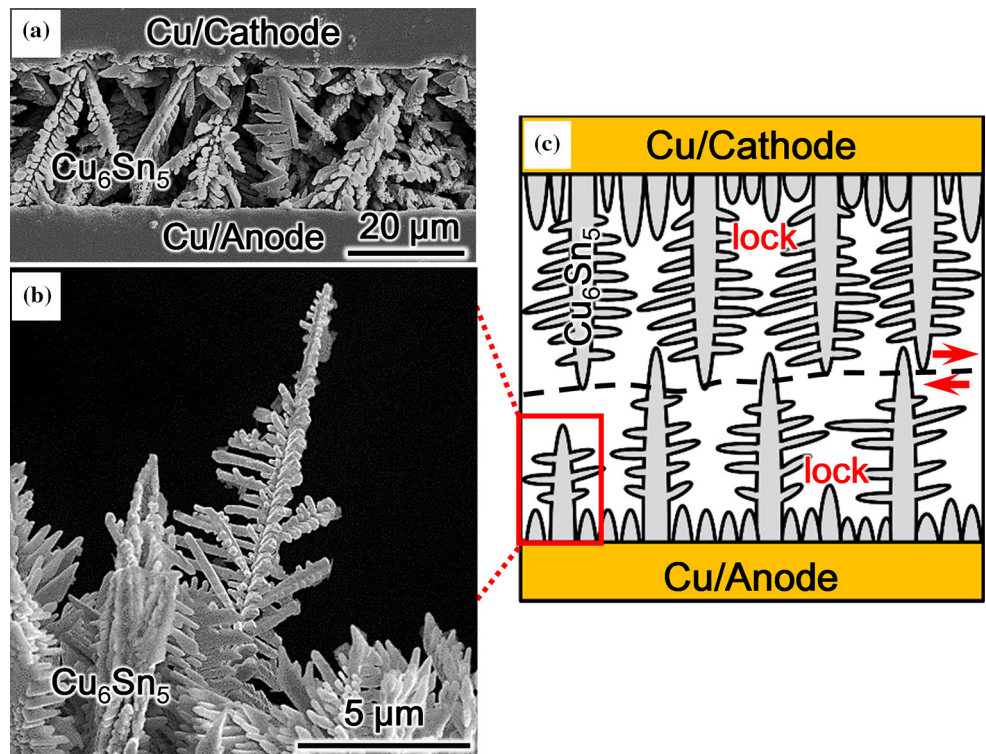


Figure 9 SEM images of the fracture surfaces at cathode side with the times of **a** 60 ms, **b** 120 ms, and **d** 180 ms.

In the Cu_6Sn_5 -based solder joint, the Cu_6Sn_5 primary-branch with protruding tips was almost perpendicular to the Cu substrates and extended into the Sn solder matrix. Under the horizontal shear loads, a crack began in the waist of the primary-branch tips and then propagated into the adjacent Sn solder, as shown in Fig. 10c. Moreover, as reported by Man et al. [47, 48], the network of dendritic Cu_6Sn_5 grains can provide extra surface area and locking mechanism for adhesion joints, leading to the increase in the joint strength. Thus, the dendritic Cu_6Sn_5 grains with densely hierarchical structure in the Cu_6Sn_5 -based solder joint contributed to higher shear strength compared to the Sn-based solder joint

with rod-like Cu_6Sn_5 . With the bonding time continuing to increase above 150 ms, the fracture mode for the Cu_3Sn -based joint was transformed into brittle type. As shown in Fig. 9c, for the Cu_3Sn joint after bonded for 180 ms, a crack occurred initially within the interior of the Cu_3Sn layer, and finally resulted in the formation of transgranular fractography. From the metallurgical point of view, when one Sn atom reacted with three Cu atoms to form the Cu_3Sn compounds, the volume reduction of 8.2 % was generated [49, 50]. The phase transformation-induced stress can thus be accumulated in the brittle Cu_3Sn compounds, resulting in the transgranular fracture within the Cu_3Sn layer.

Figure 10 **a** and **b** are the side-view SEM images of dendritic Cu_6Sn_5 grains in the deep-etched samples after 120 ms; **c** is the schematic diagram of the fracture mode for the Cu_6Sn_5 -based solder joint.



Conclusions

In this paper, the microstructural and mechanical analyses of Cu–Sn intermetallic interconnects, which were prepared by soldering Cu/Sn/Cu sandwich structures with the assistance of electric current at ambient temperature within 180 ms, are summarized below:

- (1) At the initial stage, the joule heat generated at the faying interfaces served as the main heating source to melt the solid Sn solder interlayer. Under the imposed current density of $1.44 \times 10^4 \text{ A cm}^{-2}$, the Sn-based solder joint with rod-like Cu_6Sn_5 was formed after 40 ms.
- (2) The joule heat-induced temperature coupled with the driving force of solid–liquid electromigration were both increased with the bonding times, resulting in more Cu atoms being dissolved into molten Sn solder. After 120 ms, masses of dendritic Cu_6Sn_5 grains were formed due to constitutional supercooling effect.
- (3) With the joule heat-induced temperature increased above the melting point of Cu_6Sn_5 , the dendritic Cu_6Sn_5 were melted and totally transformed into Cu_3Sn , leading to the formation of homogeneous Cu_3Sn intermetallic joint after 180 ms.
- (4) Due to the locking mechanism of Cu_6Sn_5 dendritic network, the shear strength of the resulted solder joints was increased with the bonding times. Meanwhile, the homogeneous Cu_3Sn joint exhibited the highest shear strength of 67.3 MPa.

Acknowledgements

The authors are grateful for financial support from the National Natural Science Foundation of China (Grant No. 51522503) and support from Program for New Century Excellent Talents in University (NCET-13-0175).

Compliance with ethical standards

Conflict of Interest The authors declare that they have no conflict of interest.

References

- [1] Xiao G, Yang X, Yuan G, Li Z, Shu X (2015) Mechanical properties of intermetallic compounds at the Sn–3.0Ag–0.5Cu/Cu joint interface using nanoindentation. *Mater Des* 88:520–527
- [2] Goh Y, Haseeb A, Liew HL, Sabri MFM (2015) Deformation and fracture behaviour of electroplated Sn–Bi/Cu solder joints. *J Mater Sci* 50:4258–4269. doi:10.1007/s10853-015-8978-0
- [3] Zhong WH, Chan YC, Wu BY, Alam MO, Guan JF (2007) Multiple reflow study of ball grid array (BGA) solder joints on Au/Ni metallization. *J Mater Sci* 42:5239–5247. doi:10.1007/s10853-006-1234-x
- [4] Chiu WL, Liu CM, Haung YS, Chen C (2014) Formation of nearly void-free Cu_3Sn intermetallic joints using nanotwinned Cu metallization. *Appl Phys Lett* 104:171902
- [5] Hsiao HY, Liu CM, Lin HW, Liu TC, Lu CL, Huang YS, Chen C, Tu K (2012) Unidirectional growth of microbumps on (111)-oriented and nanotwinned copper. *Science* 336:1007–1010
- [6] Huang M, Yang F (2014) Size effect model on kinetics of interfacial reaction between Sn– x Ag– y Cu solders and Cu substrate. *Sci Rep* 4:7117
- [7] Chen C, Yu D, Chen KN (2015) Vertical interconnects of microbumps in 3D integration. *MRS Bull* 40:257–263
- [8] Mo L, Chen Z, Wu F, Liu C (2015) Microstructural and mechanical analysis on Cu–Sn intermetallic micro-joints under isothermal condition. *Intermetallics* 66:13–21
- [9] Choudhury SF, Ladani L (2016) Miniaturization of micro-solder bumps and effect of IMC on stress distribution. *J Electron Mater* 45:3683–3694
- [10] Choudhury SF, Ladani L (2015) Effect of intermetallic compounds on the thermomechanical fatigue life of three-dimensional integrated circuit package micro-solder bumps: finite element analysis and study. *J Electron Packag* 137:041003
- [11] Choudhury SF, Ladani L (2016) Local shear stress-strain response of Sn–3.5Ag/Cu solder joint with high fraction of intermetallic compounds: experimental analysis. *J Alloy Compd* 680:665–676
- [12] Yang M, Li M, Wang L, Fu Y, Kim J, Weng L (2011) Cu_6Sn_5 morphology transition and its effect on mechanical properties of eutectic Sn–Ag solder joints. *J Electron Mater* 40:176–188
- [13] Mohd Salleh MAA, McDonald SD, Yasuda H, Sugiyama A, Nogita K (2015) Rapid Cu_6Sn_5 growth at liquid Sn/solid Cu interfaces. *Scr Mater* 100:17–20

- [14] Yu HB, Sun Y, Alpay S, Aindow M (2016) Solidification microstructures in $\text{Ag}_3\text{Sn}-\text{Cu}_3\text{Sn}$ pseudo-binary alloys. *J Mater Sci* 51:6474–6487. doi:[10.1007/s10853-016-9947-y](https://doi.org/10.1007/s10853-016-9947-y)
- [15] Xia Y, Xie X, Lu C (2006) Intermetallic compounds evolution between lead-free solder and Cu-based lead frame alloys during isothermal aging. *J Mater Sci* 41:2359–2364. doi:[10.1007/s10853-006-4501-y](https://doi.org/10.1007/s10853-006-4501-y)
- [16] Li M, Li Z, Xiao Y, Wang C (2013) Rapid formation of Cu/ $\text{Cu}_3\text{Sn}/\text{Cu}$ joints using ultrasonic bonding process at ambient temperature. *Appl Phys Lett* 102:094104
- [17] Li Z, Li M, Xiao Y, Wang C (2014) Ultrarapid formation of homogeneous Cu_6Sn_5 and Cu_3Sn intermetallic compound joints at room temperature using ultrasonic waves. *Ultrason Sonochem* 21:924–929
- [18] Cheng HC, Yu CF, Chen WH (2012) Strain- and strain-rate-dependent mechanical properties and behaviors of Cu_3Sn compound using molecular dynamics simulation. *J Mater Sci* 47:3103–3114. doi:[10.1007/s10853-011-6144-x](https://doi.org/10.1007/s10853-011-6144-x)
- [19] Li J, Agyakwa P, Johnson C (2011) Interfacial reaction in Cu/Sn/Cu system during the transient liquid phase soldering process. *Acta Mater* 59:1198–1211
- [20] Zhang R, Tian Y, Hang C, Liu B, Wang C (2013) Formation mechanism and orientation of Cu_3Sn grains in Cu–Sn intermetallic compound joints. *Mater Lett* 110:137–140
- [21] Hang C, Tian Y, Zhang R, Yang D (2013) Phase transformation and grain orientation of Cu–Sn intermetallic compounds during low temperature bonding process. *J Mater Sci* 24:3905–3913. doi:[10.1007/s10854-013-1337-5](https://doi.org/10.1007/s10854-013-1337-5)
- [22] Ji H, Qiao Y, Li M (2015) Rapid formation of intermetallic joints through ultrasonic-assisted die bonding with Sn–0.7 Cu solder for high temperature packaging application. *Scripta Mater* 110:19–23
- [23] Ma H, Kunwar A, Sun J, Guo B, Ma H (2015) In situ study on the increase of intermetallic compound thickness at anode of molten tin due to electromigration of copper. *Scr Mater* 107:88–91
- [24] Gu Y, Shen P, Yang NN, Cao KZ (2014) Effects of direct current on the wetting behavior and interfacial morphology between molten Sn and Cu substrate. *J Alloy Compd* 586:80–86
- [25] Liu C, Hu Y, Liu Y, Tseng H, Huang T, Lu C, Chuang Y, Cheng S (2013) Epitaxial Cu–Sn bulk crystals grown by electric current. *Acta Mater* 61:5713–5719
- [26] Huang J, Tsai C, Lin Y, Kao C (2008) Pronounced electromigration of Cu in molten Sn-based solders. *J Mater Res* 23:250–257
- [27] Huang ML, Zhou Q, Zhao N, Liu XY, Zhang ZJ (2014) Reverse polarity effect and cross-solder interaction in Cu/ $\text{Sn}-9\text{Zn}/\text{Ni}$ interconnect during liquid-solid electromigration. *J Mater Sci* 49:1755–1763. doi:[10.1007/s10853-013-7862-z](https://doi.org/10.1007/s10853-013-7862-z)
- [28] Zhou Y, Gorman P, Tan W, Ely K (2000) Weldability of thin sheet metals during small-scale resistance spot welding using an alternating-current power supply. *J Electron Mater* 29:1090–1099
- [29] Tan W, Zhou Y, Kerr H, Lawson S (2004) A study of dynamic resistance during small scale resistance spot welding of thin Ni sheets. *J Phys D Appl Phys* 37:1998
- [30] Munir ZA, Quach DV, Ohyanagi M (2011) Electric current activation of sintering: a review of the pulsed electric current sintering process. *J Am Ceram Soc* 94:1–19
- [31] Munir Z, Anselmi TU, Ohyanagi M (2006) The effect of electric field and pressure on the synthesis and consolidation of materials: a review of the spark plasma sintering method. *J Mater Sci* 41(3):763–777. doi:[10.1007/s10853-006-6555-2](https://doi.org/10.1007/s10853-006-6555-2)
- [32] Ke JH, Chuang HY, Shih WL, Kao CR (2012) Mechanism for serrated cathode dissolution in Cu/Sn/Cu interconnect under electron current stressing. *Acta Mater* 60:2082–2090
- [33] Liu C, Chen J, Chuang Y, Ke L, Wang S (2007) Electromigration-induced Kirkendall voids at the Cu/ Cu_3Sn interface in flip-chip Cu/Sn/Cu joints. *Appl Phys Lett* 90:2114
- [34] Wang YW, Lin YW, Kao CR (2009) Kirkendall voids formation in the reaction between Ni-doped SnAg lead-free solders and different Cu substrates. *Microelectron Reliab* 49:248–252
- [35] Knödler H (1957) Der strukturelle Zusammenhang zwischen γ -und ϵ -Phase im System Kupfer-Zinn. *Acta Crystallogr* 10:86–87
- [36] Kim H, Tu K (1996) Kinetic analysis of the soldering reaction between eutectic SnPb alloy and Cu accompanied by ripening. *Phys Rev B* 53:16027
- [37] Zou HF, Yang HJ, Zhang ZF (2008) Morphologies, orientation relationships and evolution of Cu_6Sn_5 grains formed between molten Sn and Cu single crystals. *Acta Mater* 56:2649–2662
- [38] Tian Y, Zhang R, Hang C, Niu L, Wang C (2014) Relationship between morphologies and orientations of Cu_6Sn_5 grains in Sn3.0 Ag0.5 Cu solder joints on different Cu pads. *Mater Charact* 88:58–68
- [39] Reed T, LaFleur W (1964) Constitutional supercooling in iodine vapor crystal growth. *Appl Phys Lett* 5:191–193
- [40] Jackson KA (2004) Constitutional supercooling surface roughening. *J Cryst Growth* 264:519–529
- [41] Ben JE, Garik P (1990) The formation of patterns in non-equilibrium growth. *Nature* 343:523–530
- [42] Tiller WA, Jackson KA, Rutter JW, Chalmers B (1953) The redistribution of solute atoms during the solidification of metals. *Acta Mater* 1:428–437
- [43] Cheng T (2000) The mechanism of grain refinement in TiAl alloys by boron addition—an alternative hypothesis. *Intermetallics* 8:29–37

- [44] Xian JW, Belyakov SA, Britton TB, Gourlay CM (2015) Heterogeneous nucleation of Cu_6Sn_5 in Sn–Cu–Al solders. *J Alloy Compd* 619:345–355
- [45] Zhao J, Cheng CQ, Qi L, Chi CY (2009) Kinetics of intermetallic compound layers and shear strength in Bi-bearing SnAgCu/Cu soldering couples. *J Alloy Compd* 473:382–388
- [46] Pang HLJ, Tan KH, Shi XQ, Wang ZP (2001) Microstructure and intermetallic growth effects on shear and fatigue strength of solder joints subjected to thermal cycling aging. *Mat Sci Eng A-Struct* 307:42–50
- [47] Man HC, Zhao NQ (2006) Enhancing the adhesive bonding strength of NiTi shape memory alloys by laser gas nitriding and selective etching. *Appl Surf Sci* 253:1595–1600
- [48] Man H, Zhao N, Cui Z (2005) Surface morphology of a laser surface nitrided and etched Ti-6Al-4 V alloy. *Surf Coat Tech* 192:341–346
- [49] Mei Z, Sunwoo A, Morris J (1992) Analysis of low-temperature intermetallic growth in copper-tin diffusion couples. *Metall Mater Trans A* 23:857–864
- [50] Lee HT, Chen MH, Jao HM, Liao TL (2003) Influence of interfacial intermetallic compound on fracture behavior of solder joints. *Mat Sci Eng A-Struct* 358:134–141